# INJECTION PHOTODIODE BASED ON AN Al–p-Si–n-$Zn_{85}Mg_{15}O$–n-$Zn_{65}Mg_{35}O$–Ag STRUCTURE

V. MORARI[1], E. V. RUSU[1], V. POSTOLACHE[2], V. V. URSAKI[2], I. M. TIGINYANU[2], A. V. ROGACHEV[3], A. V. SEMCHENKO[3]

[1] D. Ghitu Institute of Electronic Engineering and Nanotechnology, MD-2028 Chisinau, Republic of Moldova
[2] National Center for Materials Study and Testing, Technical University of Moldova, MD-2004 Chisinau, Republic of Moldova
*E-mail:* vvursaki@gmail.com
[3] Francisk Skorina Gomel State University, Gomel, 246019, Republic of Belarus

*Received April 22, 2021*

*Abstract*. A series of $Zn_{1-x}Mg_xO$ thin films with the composition range $x = 0.00–0.60$ has been prepared by aerosol spray pyrolysis deposition on Si or quartz substrates. The morphology, composition, crystals structure, and optical properties of the prepared films were studied by *scanning electron microscopy* (SEM), *energy dispersive X-ray analysis* (EDX), *X-ray diffraction* (XRD), and optical spectroscopy. It was found that the morphology of films is not significantly different for films with different compositions, while the compositions correspond to those preset in the spray solutions, and all the films are of wurtzite structure up to the $x$ value of 0.6. The optical bandgap of films was determined from the absorption spectra, and the dependence of the bandgap on the Mg content was compared with previously reported data. A photodetector with a design composed of two $Zn_{1-x}Mg_xO$ layers with different compositions was developed and characterized. It was found that the photodetector operates as injection photodiode with improved parameters as compared to a previous device with a single ZnMgO film prepared by spin coating.

*Key words*: Thin ZnMgO films, aerosol spray pyrolysis, photodetector, current-voltage characteristic, injection photodiode.

## 1. INTRODUCTION

Due to its suitable for applications optical and electrical properties (wide bandgap of ~3.36 eV, large exciton binding energy of ~60 meV, high electron mobility, high optical transparency, and low cost) the wurtzite zinc oxide become a technologically important material for a wide range of applications, such as UV *light-emitting diodes* (LEDs) [1, 2], lasers [3–8], photodetectors [9–13], solar cells [14–16], gas sensors [17, 18], and transparent electronics [19]. Some of these applications, particularly photodetectors and light emitting devices, require means of changing the material bandgap, in order to tune the spectral range of emission or optical sensitivity.

Alloying with Mg in ZnMgO solid solutions offers a possibility to tailor many important physical properties by varying their composition. This alloy system covers a wide *ultraviolet* (UV) spectral range between the direct bandgaps of 3.36 eV for ZnO and 7.8 eV for MgO at room temperature.

ZnMgO films have been previously prepared by a variety of technological methods such as radio-frequency [10, 12] and direct current [20] magnetron sputtering, *radio-frequency plasma-assisted molecular beam epitaxy* (RF-MBE) [11, 21, 22], *plasma-enhanced atomic layer deposition* (PE-ALD) [23], *pulsed laser deposition* (PLD) [24], *metal–organic chemical vapor deposition* (MOCVD) [25], *chemical bath deposition* (CBD) [26], spray pyrolysis [22, 27] and sol–gel spin coating [28, 29]. The last three techniques are more advantageous from the point of view of simplicity and processing cost. Recently performed studies revealed that the sensitivity of photodetectors in the metal semiconductor metal configuration with ZnMgO films prepared by spin coating and Pd contacts is higher as compared to those obtained by spray pyrolysis [30]. On the other hand, the photoresponse to UV irradiation is faster for films prepared by spray pyrolysis.

Concerning photodiodes with p-n heterojunction, apart from classical devices operating at reverse bias, photodiodes operating in the mode of internal amplification of the primary photocurrent at both reverse and forward biases have been demonstrating with more complex structures consisting of several semiconductor layers [31–33]. It has been found that reversal of photocurrent occurs in such structures at low luminance levels and low forward bias voltage making it possible to develop selective photodetectors with injection properties. At high forward bias voltage of these structures, they also operate as injection photodiodes and exhibit a much higher integrated sensitivity as compared to diodes operating in the traditional mode with the reverse direction of the photocurrent. Working of p-Si/n-$Zn_{1-x}Mg_xO$ heterojunctions with ZnMgO films prepared by spin coating as injection photodiodes has also been demonstrated at low forward bias voltage of 0.1–1.0 V [34]. However, it was found that the ratio of photocurrent to the dark current decreases with increasing the forward bias voltage.

The goal of this paper is to elaborate a photodetector on the basis of $Zn_{1-x}Mg_xO$ films prepared by aerosol spray pyrolysis deposition on Si substrates operating as injection photodiodes al higher forward bias voltage.

## 2. SAMPLE PREPARATION AND EXPERIMENTAL DETAILS

A solution has been prepared from 99.999% purity zinc acetate dihydrate and 99% purity magnesium acetate tetrahydrate dissolved in ethanol. The prepared solution was sprayed onto the Si(111) substrate by means of a homemade sprayer using an oxigen gas flow. 0.35 M zinc acetate and magnesium acetate solutions were mixed during 30 minutes at a temperature of 50–60°C in an ultrasonic bath in various proportions to produce ZnMgO films with Mg content from 0% to 60%. The substrate was heated at the temperature of 500°C during the deposition. The distance between the sprayer and the heated substrate was kept at 18 cm to produce a uniform coverage of the film on the substrate. The solution was injected into the oxygen gas flow by means of a syringe controlled by a stepper motor *via* a computer interface. The produced film thickness is determined by the rate of precursor solution injection and the duration of deposition process. An injection rate of 0.33 mL/min was used to produce films with needed thickness with the duration of the deposition process of 15 min.

For optical characterization, similar films were deposited onto quartz substrates and optical transmission spectra were measured at room temperature with a Jasco V-670 spectrometer.

The morphology and chemical composition of the produced films were studied with a LEO-ZEISS Gemini 1530 scanning electron microscope equipped with tools for *energy dispersive X-ray analysis* (EDX). *X-ray diffraction* (XRD) measurements were carried out on a Rigaku SmartLab X Ray Diffractometer using $CuK_\alpha$ radiation ($\lambda = 0.15406$ nm).

For the preparation of an Al–p-Si–n-$Zn_{85}Mg_{15}O$–n-$Zn_{65}Mg_{35}O$–Ag heterostructure photodetector, the Al ohmic contact was deposited by thermal evaporation on the backside of the Si substrate. The front-side contacts were fabricated by deposition of an Ag film on the surface of the $Zn_{65}Mg_{35}O$ film through a special mask with heating the sample at the temperature of 300°C in vacuum. The current–voltage characteristics of the photodetector structure were measured with a Keithley 2400 *Source Meter Unit* (SMU), while the photocurrent was generated by a xenon DKSS-150 lamp passed though different optical filters.

## 3. MORPHOLOGY, COMPOSITION AND CRYSTAL STRUCTURE CHARACTERIZATION OF THE PREPARED FILMS

Apart from the ZnMgO films with the Mg content of 15% and 35% implemented in the photodetector device, films with other compositions were prepared for a wider characterization. Figure 1 illustrates the morphology of two films with the composition of $Zn_{0.80}Mg_{0.2}O$ and $Zn_{0.6}Mg_{0.4}O$. The SEM images with low magnification demonstrate the uniformity of films over a large surface, while the cross section images with higher magnification show that the films with thickness around 300 nm have a dense packing of nanocrystals. The sizes of nanocrystallites as well as the surface morphology on the frontal SEM images are not significantly different for films with different compositions.

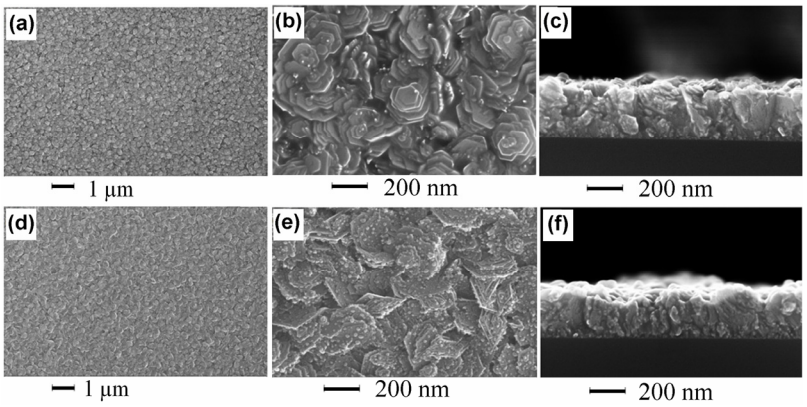


Fig. 1 – SEM images of $Zn_{0.80}Mg_{0.2}O$ (a,b,c) and $Zn_{0.6}Mg_{0.4}O$ (d,e,f) films deposited on p-Si substrates by spray pyrolysis method.

The results of the EDX analysis shown in Fig. 2 suggest that the compositions of the $Zn_{1-x}Mg_xO$ alloy films are stoichiometric and they correspond to those preset in the zinc acetate – magnesium acetate spray solutions, within the limits of the errors defined by instrumental accuracy.

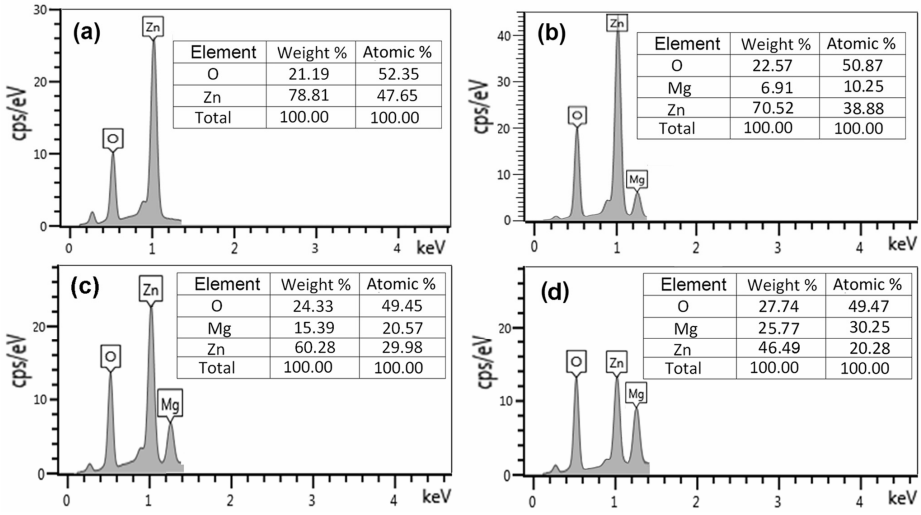


Fig. 2 – Elemental composition of a ZnO (a), $Zn_{0.8}Mg_{0.2}O$ (b), $Zn_{0.6}Mg_{0.4}O$ (c), and $Zn_{0.4}Mg_{0.6}O$ (b) films determined by EDX analysis.

The XRD pattern of a $Zn_{0.4}Mg_{0.6}O$ film (Fig. 3) revealed only reflexes related to the wurtzite ZnMgO phase (PDF Card No. 01-078-3032), demonstrating a single phase composition of the film with as high content of Mg as 60%, which is an important result suggesting existence of possibilities to avoid mixed phase compositions in the ZnMgO alloy system, or at least to strongly restrict the *x*-value range with mixed phases.

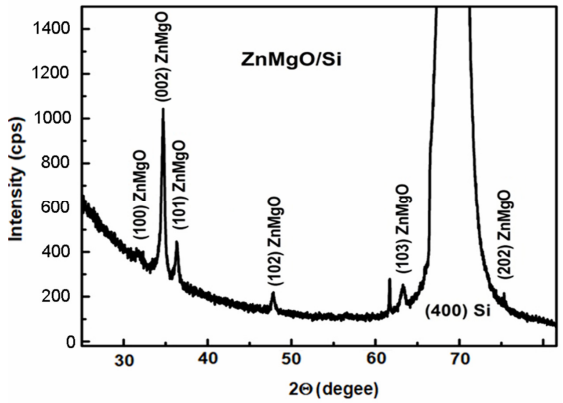


Fig. 3 – XRD pattern of a $Zn_{0.4}Mg_{0.6}O$ film deposited by spray pyrolysis methods on a Si substrate.

## 4. INVESTIGATION OF OPTICAL PROPERTIES

Concerning the optical properties, it was found that all the prepared films exhibit a fairly high transparency at a level of 80% in the visible spectral range up to 3.3 eV. The optical bandgap was deduced from the Tauc plot (Fig. 4a), and the dependence of the bandgap on the Mg content in films is shown in Fig. 4b, along with previously reported data.

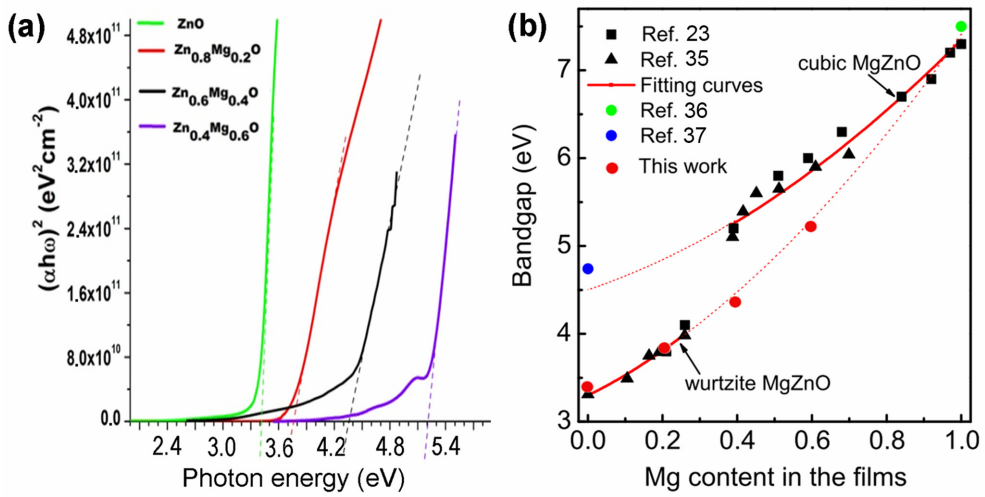


Fig. 4 – (a) Tauc plot of optical absorption spectra measured at room temperature for $Zn_{1-x}Mg_xO$ films deposited by aerosol spray pyrolysis methods on quartz substrates. (b) Dependence of the bandgap of $Zn_{1-x}Mg_xO$ films on Mg content $x$ in the films.

The experimental data concerning the dependence of the MgZnO alloys bandgap on the composition of films were fitted by a standard bowing equation as described in ref. [24]. One can observe that the experimental data are well fitted by two curves, the upper one corresponding to the cubic ZnMgO phase with the bangap value parameters of 4.44 eV and 7.30 eV for ZnO and MgO, respectively, while the lower curve is for the wurtzite ZnMgO phase with the bandgap value parameters of 3.31 eV and 7.41 eV for ZnO and MgO, respectively.

The experimental data for $Zn_{1-x}Mg_xO$ films prepared by PLD were fitted in ref. [24] by the curve corresponding to the wurtzite phase up to the $x$ value of 0.27, and by the curve corresponding to the cubic phase down to the $x$ value of 0.4. At the same time, the data of the present work show that the bandgap of films prepared by spray pyrolysis are fitted by the curve corresponding to the wurtzite phase up to the $x$ value of 0.60, which corroborates the structure deduce from the XRD pattern in Fig. 3. This is an important finding demonstrating possibilities to produce ZnMgO films with wurtzite structure up to a Mg content of 60%.

## 5. PHOTODIODE DESIGN AND CHARACTERIZATION

As mentioned above, photodiodes with injection properties working at low forward bias voltages have been demonstrated in a previous work on p-Si/ n-$Zn_{1-x}Mg_xO$ heterojunctions with ZnMgO films prepared by spin coating [34]. However, those devices had a drawback of working only up the bias of 1 V, therefore impeding achieving of high responsivity and detectivity parameters. In order to extend the forward bias operating range as well as the selectivity of the photodetector, a structure design with two $Zn_{1-x}Mg_xO$ layers with different compositions is proposed in this work as shown in Fig. 5a on the basis of films prepared by spray pyrolysis.

Apart from creating a complex band diagram, as shown in Fig. 6, the wider bandgap $Zn_{0.65}Mg_{0.35}O$ upper layer plays a role of window, which protects the UV absorbing layer with the composition of $Zn_{0.85}Mg_{0.15}O$ and reduces the density of surface states. Such a design improves the selectivity of the photodetector, which is practically insensitive to the infrared (IR) radiation, and is by a factor of 7 less sensitive to the visible radiation as compared to the UV radiation as shown in Fig. 5b.

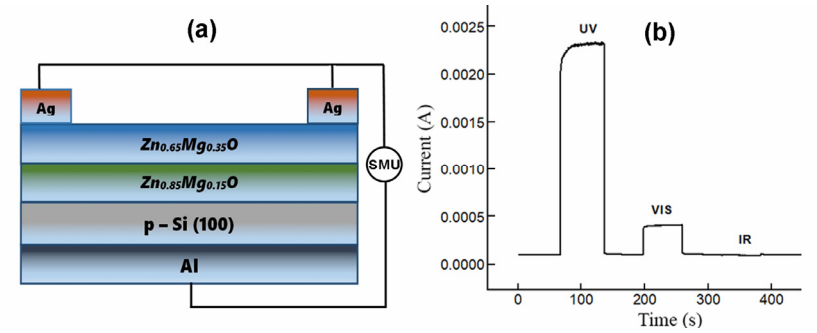


Fig. 5 – (a) Schematic diagram of an Al–p-Si–n-$Zn_{85}Mg_{15}O$–n-$Zn_{65}Mg_{35}O$–Ag photodiode. (b) The relaxation of photocurrent measured at 300 K with reverse bias voltage of 5 V under irradiation with different wavelengths.

The bandgap of Si and its electron affinity are 1.12 eV and 4.05 eV, respectively [38, 39]. The reported value of the electron affinity of ZnO is in the range of 4.0 eV to 4.5 eV [40–43], while the most accepted value is of 4.35 eV [44–46]. The electron affinity of $Zn_{1-x}Mg_xO$ solutions decreases with increasing the *x* value. The conduction band offset and the valence band offsets were calculated to increase as 1.57x and –0.79x, respectively, on the basis of density functional theory within the linear muffin-tin orbital (LMTO) approach [47], *i.e.* the band offset ratio (CBO:VBO) is about 2. The experimentally reported values of the CBO:VBO ratio vary in the range of 3:2 to 7:3 [48], or from 1.5 to 2 [49]. At Mg concentration of 15%, the calculated CBO (VBO) is 0.23 eV (0.11 eV) [10], while the experimentally measured data are of 0.16 eV (0.09 eV) [49], or 0.18 eV (0.13 eV) [50].

With a value of CBO of 0.2 eV and the electron affinity of 4.35 eV for ZnO, one can deduce the value of 4.15 eV for the electron affinity of $Zn_{0.85}Mg_{0.15}O$. The calculated value of CBO for $Zn_{0.65}Mg_{0.35}O$ is 0.55 eV [47]. With this value, the

electron affinity for the $Zn_{0.65}Mg_{0.35}O$ is estimated to be of 3.8 eV. The energy band diagrams of the p-Si–n-$Zn_{85}Mg_{15}O$–n-$Zn_{65}Mg_{35}O$ heterojunction with these data are presented in Fig. 6.

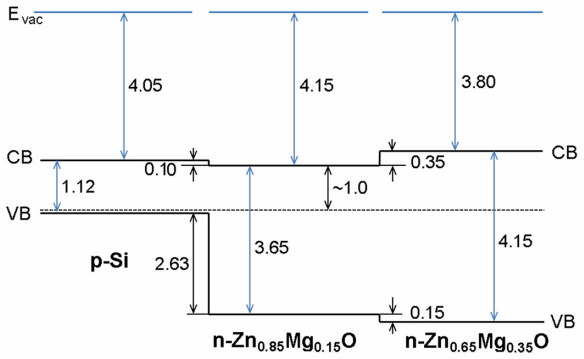


Fig. 6 – Energy band diagrams of the p-Si–n-$Zn_{85}Mg_{15}O$–n-$Zn_{65}Mg_{35}O$ heterojunction device under thermal equilibrium.

The current-voltage (I–V) characteristics of a p-Si–n-$Zn_{85}Mg_{15}O$–n-$Zn_{65}Mg_{35}O$ heterojunction device in different coordinates are presented in Fig. 7.

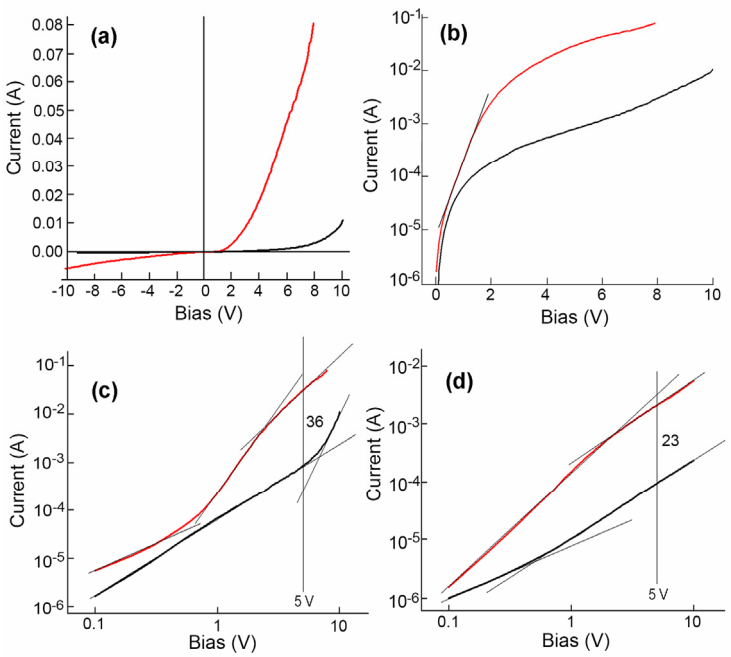


Fig. 7 – Current–voltage characteristics in dark (black line) and under UV illumination (red line) for an Al–p-Si–n-$Zn_{85}Mg_{15}O$–n-$Zn_{65}Mg_{35}O$–Ag structure plotted on linear (a), semi-logarithmic (b) and double logarithmic (c, d) coordinates at forward (b, c) and reverse (d) bias voltages.

One can see from Figure 7b that the current-voltage characteristic at forward bias voltage does not fit the classical formula for a p-n junction $I = I_S\left[\exp\left(\frac{qU}{nkT}\right)-1\right]$, since it is not a straight line in the semi-logarithmic coordinates. Only a narrow segment of the curve measured under illumination can be approximated by a straight line. Apart from that, in contrast to a classical p-n junction which works as a photodetector only at reverse bias, the investigated hetero-junction operates as photodetector at both forward and reverse bias voltages, as deduced from Figs. 7c and 7d.

The I–V characteristic fits a straight line in the double logarithmic coordinates at forward bias voltage up to 5 V in dark, therefore corresponding to a power function $I \propto U^n$, which is predicted by the Lampert theory [51]. The *n* value is about 2, which corresponds to the *space charge limited* (SCL) current injection according to the *Mott-Gurney* (MG) law [52]. It means that the investigated heterojunction works as an injection photodiode at forward bias, similarly to previously reported data on complex Si-CdS [33], CdS-CdTe [53], and CdS-CdSTe-ZnCdTe [32] heterostructures.

At reverse bias voltages, the value of the *n* parameter varies from 1 to 2 both in dark and under UV illumination, while the *n* value switches under the UV illumination from less than 2 to more than 3 at a forward bias around 0.6 V. This phenomenon significantly improves the photosensitivity of the photodetector at forward biases higher than 1 V, in contrast to previously reported injection photodiodes with a single ZnMgO layer prepared by spin coating [34]. The ratio of photocurrent to the dark current increases from 2 to 36 with increasing the forward bias from 0.6 V to 5 V, while this ratio equals 23 for the reverse bias of 5 V, *i.e.* the sensitivity of the photodetector is by a factor of 1.5 better at forward bias as compared to reverse bias.

The parameters of the photodetector (responsivity and detectivity) were calculated from the experimental data according to the formula (2) and (3), respectively [54]:

$$R = (I_{photo} - I_{dark}) / P_{ill}, \tag{2}$$

$$D^* = \frac{R\sqrt{A}}{\sqrt{2eI_{dark}}} \tag{3}$$

where $I_{photo}$ is the current under illumination, $I_{dark}$ is the current in dark, $P_{ill}$ is the illumination power, $A$ is the active area of the photodetector, and $e$ is the elementary charge.

The parameters of a device with an active area of 0.125 $cm^2$ under the UV illumination with a power of 63 mW are presented in Table 1.

*Table 1*

Parameters of an Al–p-Si–n-$Zn_{85}Mg_{15}O$–n-$Zn_{65}Mg_{35}O$–Ag photodetector

| Bias | Responsivity (R) | Detectivity ($D^*$) |
|---|---|---|
| Reverse 5V | 35 mA · $W^{-1}$ | $2 \times 10^9$ cm · $Hz^{1/2}$ · $W^{-1}$ |
| Forward 5V | 460 mA · $W^{-1}$ | $1 \times 10^{10}$ cm · $Hz^{1/2}$ · $W^{-1}$ |

## 6. CONCLUSIONS

The results of this study demonstrate the preparation of ZnMgO thin films by aerosol spray pyrolysis on Si substrates with homogeneous morphology insignificantly affected by the Mg content. The films are of wurtzite structure up to the Mg content of 60% as demonstrated by the results of XRD and optical bandgap analysis. This Mg content is higher than previously reported data for films with wurtzite structure, therefore demonstrating prospects for avoiding mixed phase alloying in the ZnMgO system, or at least to strongly restrict the composition range with mixed phases.

The analysis of the energy band diagrams of the developed p-Si–n-$Zn_{85}Mg_{15}O$–n-$Zn_{65}Mg_{35}O$ heterojunction device suggests a small conduction band offset over the heterostructures interfaces under thermal equilibrium, as well as a small valence band offset at the $Zn_{85}Mg_{15}O/Zn_{65}Mg_{35}O$ interface.

The analysis of the current-voltage characteristics in dark and under UV illumination suggests the operation of the elaborated photodetector devise in the injection photodiode mode at forward bias voltages. The operation forward bias range is significantly wider as compared to a device with a single ZnMgO film prepared by spin coating, which results in significantly improved parameters. The responsivity of 460 mA · $W^{-1}$ and detectivity of $1 \times 10^{10}$ cm · $Hz^{1/2}$ · $W^{-1}$ measured at forward bias of 5V are by an order of magnitude better than these parameters measured at the reverse bias.

*Acknowledgements.* This work supported financially by the National Agency for Research and Development of the Republic of Moldova under the grant nos. 20.80009.5007.02 and 15.817.02.06A, and by the Horizon-2020 research and innovation programme of the European Union (Grant No. 810652, NanoMedTwin project).

REFERENCES

1. B. R. Lee, E. D. Jung, J. S. Park, Y. S. Nam, S. H. Min, B.-S. Kim, K.-M. Lee, J.-R. Jeong, R. H. Friend, J.-S. Kim, S. O. Kim, M. H. Song, Nat. Commun. **5**, 4840 (2014).
2. F. Rahman, Optical Engineering **58**, 010901 (2019).
3. V. V. Ursaki, V. V. Zalamai, I. M. Tiginyanu, A. Burlacu, E. V. Rusu, C. Klingshirn, Appl. Phys. Lett. **95**, 171101 (2009).
4. V. V. Zalamai, V. V. Ursaki, C. Klingshirn, H. Kalt, G. A. Emelchenko, A. N. Redkin, Appl. Phys. B: Lasers Opt. **97**, 817–823 (2009).
5. D. Vanmaekelbergh, L. K. van Vugt, Nanoscale **3**, 2783–2800 (2011).

6. H. K. Liang, S. F. Yu, H. Y. Yang, Appl. Phys. Lett. **97**, 241107 (2010).
7. C. Y. Liu, H. Y. Xu, Y. Sun, J. G. Ma, Y. C. Liu, Optics Express **22**, 16731–16737 (2014).
8. M. Suja, S. B. Bashar, B. Debnath, L. Su, W. Shi, R. Lake, J. Liu, Sci. Rep. **7**, 2677 (2017).
9. J.-L. Yang, K.-W. Liu, D.-Z. Shen, Chin. Phys. B **26**, 047308 (2017).
10. C.-Z. Wu, L.-W. Ji, C.-H. Liu, S.-M. Peng, S.-J. Young, K.-T. Lam, C.-J. Huang, Sci. Technol. A. **29**, 03A118 (2011).
11. Y. N. Hou, Z. X. Mei, H. L. Liang, D. Q. Ye, C. Z. Gu, X. L. Du, Appl. Phys. Lett. **102**, 153510 (2013).
12. J.-S. Shiang, S. Brahma, C.-P. Liu, J.-L. Huang, Thin Solid Films **620**, 170–174 (2016).
13. S. Maity, P. P. Sahu, C. T. Bhunia, IEEE Sens. J. **18**, 6569–6575 (2018).
14. J. Huang, Z. Yin, Q. Zheng, Energy Environ. Sci. **4**, 3861–3877 (2011).
15. R. Vittal, K.-C. Ho, Renew. Sustain. Energy Rev. **70**, 920–935 (2017).
16. V. Consonni, J. Briscoe, E. Kärber, X. Li, T. Cossuet, Nanotechnology **30**, 362001 (2019).
17. G. Zheng, P. Zhu, L. Sun, J. Jiang, J. Liu, X. Wang, W. Li, AIP Adv. **6**, 125306 (2016).
18. Y.-T. Tsai, S.-J. Chang, L.-W. Ji, Y.-J. Hsiao, I.-T. Tang, H.-Y. Lu, Y.-L. Chu, ACS Omega **3**, 13798–13807 (2018).
19. L. Jiang, J. Li, K. Huang, S. Li, Q. Wang, Z. Sun, T. Mei, J. Wang, L. Zhang, N. Wang, X. Wang, ACS Omega **2**, 8990–8996 (2017).
20. D. Thapa, J. Huso, K. Miklos, P. M. Wojcik, D. N. McIlroy, J. L. Morrison, C. Corolewski, M. D. McCluskey, T. J. Williams, M. Grant Norton, L. Bergman, J. Mater. Sci.: Mater. Electron. **28**, 2511–2520 (2017).
21. W. V. Schoenfeld, M. Wei, R. C. Boutwell, H. Y. Liu, Proc. SPIE **8987**, 89871P (2014).
22. A. Hierro, G. Tabares, M. Lopez-Ponce, J. M. Ulloa, A. Kurtz, E. Munoz, V. Marin-Borras, V. Munoz-Sanjose, J. M. Chauveau, Proc. SPIE **9749**, 97490W (2016).
23. H.-Y. Lee, W.-H. Tsai, Y.-C. Lin, C.-T. Lee, J. Vac. Sci. Technol. B **34**, 051207 (2016).
24. X. Wang, K. Saito, T. Tanaka, M. Nishio, T. Nagaoka, M. Arita, Q. Guo, Appl. Phys. Lett. **107**, 022111 (2015).
25. L. K. Wang, Z. G. Ju, J. Y. Zhang, J. Zheng, D. Z. Shen, B. Yao, D. X. Zhao, Z. Z. Zhang, B. H. Li, C. X. Shan, Appl. Phys. Lett. 2009, 95, 131113 (2009).
26. S. Chawla, K. Jayanthi, H. Chander, Phys. Status Solidi A **205**, 271–274 (2008).
27. N. Winkler, R. A. Wibowo, W. Kautek, T. Dimopoulos, J. Mater. Chem. C **7**, 3889–3900 (2019).
28. Q. Zhang, X. Gu, Q. Zhang, J. Jiang, X. Jin, F. Li, Z. Chen, F. Zhao, Q. Li, Opt. Mater. Express **8**, 909–918 (2018).
29. C.-Y. Tsay, S.-T. Chen, M.-T. Fan, Coatings **9**, 277 (2019).
30. V. Morari, V. Postolache, G. Mihai, E. Rusu, E. Monaico, V. V. Ursachi, K. Nielsch, I. M. Tiginyanu, 4th International Conference on Nanotechnologies and Biomedical Engineering, IFMBE; I. M. Tiginyanu, V. Sontea, Eds.; Springer Nature: Switzerland, 105–109 (2020).
31. V. V. Losev, Semiconductors **43**, 1700–1703 (2009).
32. S. A. Mirsagatov, A. Y. Leiderman, O. K. Ataboev, Phys. Solid State **55**, 1635–1646 (2013).
33. S. A. Mirsagatov, I. B. Sapayev, Semiconductors **48**, 1363–1369 (2014).
34. V. Morari, A. Pantazi, N. Curmei, V. Postolache, E. V. Rusu, M. Enachescu, I. M. Tiginyanu, V. V. Ursaki, Beilstein J. Nanotechnol. **11**, 899–910 (2020).
35. X. Wang, K. Saito, T. Tanaka, M. Nishio, Q. X. Guo, J. Alloys Compd. **627**, 383–387 (2015).
36. S.-H. Jang and S. F. Chichibu, J. Appl. Phys. **112**, 073503 (2012).
37. H. Q. Ni, Y. F. Lu, Z. M. Ren, J. Appl. Phys. **91**, 1339–1343 (2002).
38. W. R. Fahrner 2011 *Amorphous Silicon/Crystalline Silicon heterojunction solar cells*, New York: Springer briefs in Applied Sciences and Technology, 2013.
39. B. Hussain, A. Aslam, T. M. Khan, M. Creighton, B. Zohuri, Electronics **8**, 238 (2019).
40. S. Vallisree, R. Thangavel, T. R. Lenka, Mater. Res. Express **6**, 025910 (2019).
41. U. Saha, M. K. Alam, RSC Advances **7**, 4806–4814 (2017).
42. I. Bouchama, S. A. Saoucha, Optik **144**, 370–377 (2017).
43. S. R. Meher, L. Balakrishnan, Z. C. Alex, Superlattices Microstruct. **100**, 703–722 (2016).

44. P. Aurang, O. Demircioglu, F. Es, R. Turan, H. E. Unalan, J. Am. Ceram. Soc. **96**, 1253–1257 (2013).
45. J. A. Aranovich, D. Golmayo, A. L. Fahrenbruch, R. H. Bube, J. Appl. Phys **51**, 4260–4268 (1980).
46. M. Dutta, D. Basak, Appl. Phys. Lett. **92**, 212112 (2008).
47. H. Yin, J. Chen, Y. Wang, J. Wang, H. Guo, Scientific Reports **7**, 41567 (2017).
48. G. Coli, K. K. Bajaj, Appl. Phys. Lett. **78**, 2861–2863 (2001).
49. H. H. Zhang, X. H. Pan, B. Lu, J. Y. Huang, P. Ding, W. Chen, H. P. He, J. G. Lu, S. S. Chen, and Z. Z. Ye, Phys. Chem. Chem. Phys. **15**, 11231–11235 (2013).
50. S. C. Su, Y. M. Lu, Z. Z. Zhang, C. X. Shan, B. H. Li, D. Z. Shen, B. Yao, J. Y. Zhang, D. X. Zhao, X. W. Fan, Appl. Phys. Lett. **93**, 082108 (2008).
51. M. A. Lampert, Rep. Prog. Phys. **27**, 329–368 (1964).
52. N. F. Mott, R. W. Gurney, *Electronic processes in ionic crystals*, second ed., Oxford Clarendon Press, 1948.
53. Sh. A. Mirsagatov, R. R. Kabulov, M. A. Makhmudov Semiconductors **47**, 825–830 (2013).
54. V. P. Sirkeli, O. Yilmazoglu, A. S. Hajo, N. D. Nedeoglo, D. D. Nedeoglo, S. Preu, F. Kuppers, H. L. Hartnagel, Phys. Status Solidi RRL **2017**, 1700418 (2017).